IEEE Access
Multidisciplinary | Rapid Review | Open Access Journal

Received 19 April 2024, accepted 29 April 2024, date of publication 27 May 2024, date of current version 3 June 2024.

Digital Object Identifier 10.1109/ACCESS.2024.3406264

RESEARCH ARTICLE

Rotation Elastogram Estimation Using Mechanical Assisted Spatial Compounding: An Experimental Validation Study

TERESA ZAGAGLIONI[1], MIGUEL TREJO[2], DAVID A. ESPÍNDOLA[3], AND BELFOR A. GALAZ[1]

[1]Departamento de Física, Universidad de Santiago de Chile, Santiago 9170124, Chile
[2]Instituto de Física de Buenos Aires (IFIBA-CONICET), Departamento de Física, Facultad de Ciencias Exactas y Naturales, Universidad de Buenos Aires, Ciudad Universitaria, Buenos Aires C1428, Argentina
[3]Instituto de Ciencias de la Ingeniería, Universidad de O'Higgins, Rancagua 2841959, Chile

Corresponding author: Belfor A. Galaz (belfor.galaz@usach.cl)

This work was supported by the Dirección de Investigaciión Científica y Tecnoliógica (DICYT),-Usach under Grant 042131GD. The work of David A. Espíndola was supported by the Fondecyt Regular from Agencia Nacional de Investigación y Desarrollo (ANID) under Grant 1190212.

ABSTRACT In quasi-static ultrasound elastography, breast tumor classification can be performed by using the rotation fill-in signature present in the rotation elastogram. This rotation fill-in signature is a benign tumors marker obtained from lesion rotation as a product of the lateral asymmetric stress field. However, the well-known low lateral resolution limitation of ultrasound imaging devices reduces the image quality of the rotation elastograms. Studies using beam-steering, synthetic transmit aperture (STA), diverging beam with STA, and sub-pitch translation of the ultrasonic beam methods have shown that the rotation elastogram's quality can be significantly improved. In this context, we aim to study the feasibility of improving the rotation elastogram quality by mechanical-assisted spatial compounding of displacement images from different ultrasound probe angles. Recently, through numerical simulations, we have shown the theoretical feasibility of this technique. Here, we present the corresponding experimental validation by using tissue-mimicking gelatin phantoms. Our experimental results show that the contrast-to-noise ratio of the rotation elastogram can be improved by approximately 5 dB by increasing the number of displacement images used in the spatial compounding for small scanning angles of about 1°. This result confirms the prediction of previous numerical simulations. In addition, we show that the estimation of rotation can be used, in conjunction with the shear strain, to compute a new parameter to quantify the rotation possibility of the inclusion with respect to its shearing nature. In conclusion, our method is technically feasible but requires an exhaustive ultrasound probe position control in synchronism with the ultrasound image acquisition process.

INDEX TERMS Quasi-static ultrasound elastography, rotation elastogram, Shear strain elastogram, spatial compounding.

I. INTRODUCTION

In quasi-static ultrasound elastography (QUE) of breast lesions, an effective image of a lesion's rotation, the so-called Rotation Elastogram (RE) [1], [2], allows performing a breast tumor classification by using a benign tumor marker called rotation fill-in [3], [4], [5]. This arises from benign breast lesions when the assumption of circularly-symmetric inclusions is extended to elliptical non-axially oriented inclusions (asymmetric). This extension has been motivated by the fact that fibroadenomas represent the most common breast lesion in young patients and more than half of benign breast biopsies [6], [7]. In addition, fibroadenomas are known to be ''wider-than-taller'' in sonographic appearance [2], [3], [6]. Since benign breast lesions tend to be loosely bound to host tissue, the rotation fill-in signature is a manifestation of the lesion slipping and rotation as a consequence of the asymmetrical stress distribution around the lesion. This asymmetry is introduced by the non-normal orientation of the benign lesion with respect to the compression axis [3], [8].

The associate editor coordinating the review of this manuscript and approving it for publication was Chao Zuo.

Conversely, malignant breast lesions tend to be firmly bound to the host tissue due to their irregular and spiculated shape, which prevents rotation under compression. On the other hand, the computation of RE images requires incorporating the lateral shear strain component, which, due to the well-known limited lateral resolution of ultrasonic images, increases the noise in the RE images. In this context, other imaging strategies such as beam-steering, synthetic transmit aperture (STA), and diverging beam with STA methods have shown that the noise in the RE images can be significantly reduced, increasing the quality of the rotation fill-in pattern [2], [9], [10], [11]. Another way of improving the RE image quality is by increasing the number of A-lines. In fact, some studies have shown that new A-lines can be incorporated by a sub-pitch translation of the ultrasonic beam or the ultrasound (US) probe itself [12], [13]. Other techniques, such as the use of dynamic programming elastography in conjunction with Horn-Schunck optical flow estimation [14], Kalman and nonlinear complex diffusion filters [15], beamforming with transverse oscillations [16], [17], and 2D strain tensor regularization method [18], may also be used to improve the rotation elastogram quality.

We recently presented a numerical study evaluating the feasibility of RE image quality improvements using a mechanical-assisted spatial compounding of displacement images from different US probes angles [19]. Similar beam-steering [2], in which the ultrasound beam is electronically steered by conveniently changing the phase of the emitted pulse for each element, our method proposes physical rotations of the US probe to change the ultrasound beam angle. Simultaneously, a quasi-static and small compression is applied for each ultrasound probe angle to obtain the displacement images [20]. First, we performed Finite Element Method (FEM) simulations in ANSYS software (ANSYS, Inc. Headquarters, Canonsburg, PA, USA) for a loosely-bond inclined elliptical inclusion, using a simple friction model without dependence on the pre-stress distribution. In this FEM simulation, a small quasi-static compression was applied at different US probe angles. The output of the FEM simulation was then coupled with the open software FIELD II (Center for Fast Ultrasound Imaging, DTU Health Technology, Lyngby Denmark) [21], [22] to simulate the corresponding ultrasound images of the pre- and post-compression states. Once the pre- and post-compression US images were computed, a 2D block matching algorithm described in [3] was used to estimate the displacement images for each US probe angle. Using a transformation coordinate matrix [2], the displacement images were accumulated to produce the pair of axial and lateral high-resolution displacement images. Thus, the RE images were computed, and its elastographic contrast-to-noise ratio (CNR_e) was studied in terms of the maximal US probe angle and the number of images used in the spatial displacement compounding. The results showed that the CNR_e of the RE image could be significantly improved by increasing the number of displacement images used in the spatial displacement compounding for US probe angles of $\approx 1.5°$.

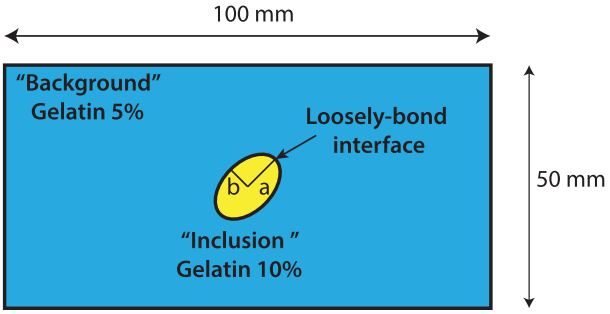

FIGURE 1. Tissue-mimicking phantom scheme. The 2D benign tumor model consists of a rectangular gelatin phantom of 5% of concentration and 106 mm× 100 mm × 50 mm dimensions. To emulate the tumor, we use a hard cylindrical inclusion with an elliptical cross-section with a gelatin concentration of 10% with major radius $a = 8$ mm and minor radius $b = 5$ mm. The inclusion is loosely-bond to background material, and its major radius is oriented to about 45° with respect to the axial direction.

In this study, we present the experimental validation of our previous numerical results by using a 2D gelatin phantom (with a harder gelatin inclusion) with a mechanical-assisted system to apply the compression at different US probe angles. The spatial displacement compounding process was performed similarly to the one used in our simulation study [19]. However, a translation component must be included in order to consider the spatial translation of the ultrasound coordinate system as a consequence of the use of a rotation axis different than the center of the transducer coordinate system. Our experimental results confirm that the contrast-to-noise ratio of the rotation elastogram can be significantly improved by increasing the number of displacement images used in the spatial compounding for small US probe angles. In addition, the improvement of lateral displacement resolution allows estimating the shear strain elastogram (*SSE* image), which is used in conjunction with the rotational to present a new parameter to evaluate the mobility of the inclusion with respect to its shearing features.

II. MATERIALS AND METHODS

A. SAMPLE PREPARATION AND EXPERIMENTAL SETUP

A 2D tissue-mimicking phantom (Figure 1) was prepared by mixing 5% concentration by weight (w/c) of gelatin (type B, bloom $\approx$ 225, Sigma Aldrich, Burlington, MA, USA) into 600 mL of distilled water. Once the gelatin powder was dissolved at 75°C, the mixture was cooled down to 45°C, and a 5% of 75 μm mean diameter glass beads (Sigma Aldrich, Burlington, MA, USA) were poured to act as scatters and produce acoustic contrast into the phantom. After pouring the glass beads, the gelatin mixture was placed into an adequately sealed rectangular mold of 106 mm×100 mm×50 mm. To ensure a homogeneous distribution of scatters (glass beads), the phantom was mounted on a rotatory system until its solidification. To emulate 2D tumors, cylindrical hard gelatin inclusions of elliptical shape were prepared

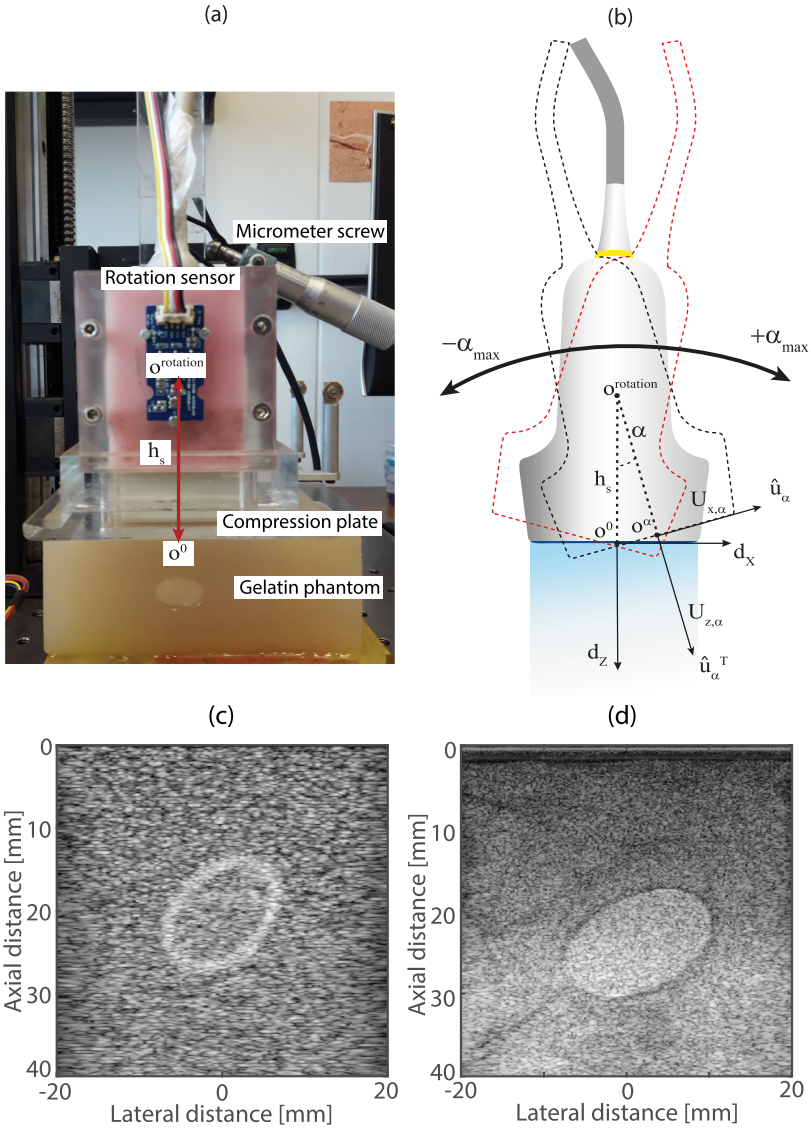

FIGURE 2. Experimental setup and spatial image compounding scheme. (a) Quasi-static ultrasound elastography imaging setup used to capture pre- and post-compression RF-raw data at different US probe tilt angles α. (b) Representative scheme showing the different coordinate systems used in the spatial compounding of several low-resolution displacement images between the range $[-\alpha_{max}, +\alpha_{max}]$. Note that figure (b) does not show the axial translation u_p^{α} introduced by the pre-compression. (c) B-mode image at $\alpha = 0°$ from simulation study [19]. (d) B-mode image at $\alpha = 0°$ from experimental study.

by using ABS plastic molds fabricated by a 3D printer (Flashforge Dreamer, Zhejiang Flashforge 3D Technology Co., Ltd, Jinhua, Zhejiang, China) and waterproofed with enamel paint. Two molds were fabricated: a cylinder (of major radius $a = 8$ mm, minor radius $b = 5$ mm and 106 mm of length) and a rectangular mold with a cylindrical hole of slightly smaller size. The first ABS mold was fixed inside the rectangular mold at an inclination of $\theta \approx 45°$ and then used to create the hole inside the rectangular soft phantom. The second ABS mold was used to pour a gelatin-distilled-water mixture of 10% of w/c and 5% glass beads to create a hard, loosely-bound elliptical inclusion. The same protocol of gelatin phantom preparation was used in [23] and described in [3] and [24], where the gelatin concentration ratio controlled the inclusion/background contrast modulus. We expected an inclusion-matrix elastic modulus ratio of about 2 for our samples.

The experimental validation was performed by using the quasi-static ultrasound elastographic setup shown in Figure 2a. An ultrasound linear array probe (Terason 12L5-V, 128 elements, 9 MHz of central frequency, Burlington, MA, USA) was fixed into an acrylic box attached to a rotation stage (RP01, Thorlabs Inc., Newton, NJ, USA), which was controlled manually through a micrometer screw in order to

impose a US probe angle α. The rotation stage was mounted on a motorized linear translation stage (WN230TA50M, Winner Optical Instruments Group Company Ltd., Beijing, China), which compresses the gelatin phantom in a controlled manner along its displacement axis, using the motion controller (WNMPC07, Winner Optical Instruments Group Company Ltd., Beijing, China). For each US probe angle α, a pre-compression of $\epsilon_p^\alpha = (W/2L)\tan(\alpha)$ was applied to avoid the loss of contact between the US probe and the phantom (W is the probe width and L is the sample length). This pre-compression was applied by a translation stage attached to a 70 mm× 50 mm compression plate mounted at the bottom of the acrylic box. After the pre-compression, a uniform axial compression $\epsilon_0 \approx 1.5$ % was applied. The ultrasound probe was driven by a Terason ultrasound scanner (Terason T3000 Advanced, Burlington, MA, USA) controlled by Matlab (R2019a, MathWorks, Natick, MA, USA) and used to acquire the beamformed radio-frequency (RF) raw data in a quasi-static manner and synchronized with the applied axial compression ϵ_0. For each angle α, a cine-loop of beamformed RF raw data was acquired before and after the axial compression ϵ_0. The Terason ultrasonic machine uses a delay-and-sum beamforming process. The pre and post-deformation cine-loops of beamformed RF raw data were acquired using the highest frequency available (12 MHz) to improve the resolution, single focus to avoid a frame rate reduction, and an acquisition depth adjusted according to phantom length. The static angle α was estimated from the accelerations measured by an inertial sensor with nine degrees-of-freedom (Grove-IMU 9DOF v1.0 with motion tracking module MPU-9150, InvenSense Inc., CA, USA) mounted on the acrylic box at the rotation coordinate system $O^{rotation}$, which was placed axially at $h_s = 3$ cm over the US probe coordinate system O^α (Figure 2a). The inertial sensor was placed with its x-axis along the gravitational force, allowing to estimate the US probe angle $\alpha = \arctan(a_y/\sqrt{a_y^2 + a_z^2})$, where a_y and a_z are the measured accelerations along the orthogonal plane of the gravitational force. Despite the high resolution of this sensor (16 bits for a range between ± 2 g to ± 16 g along the 3-axis), the environmental mechanical noise became relevant for small angle measurements (step $\Delta\alpha = 0.02°$). To reduce this, the experimental setup was mounted on an optical table, and the accelerations were averaged during 10 seconds of static capture, which allowed us to achieve a precision of 5%. The gelatin concentrations, the axial compression and the shape of the inclusion were set to maintain coherence with our previous numerical study.

For each US probe angle α, the axial and lateral displacement images, $u_{z,\alpha}$ and $u_{x,\alpha}$ (shown respectively in Figures 3a and 3b), were computed by using a multilevel, coarse-to-fine, 2-D block-matching algorithm described in [3], [19], and [25]. The displacement images were computed from the ultrasonic raw RF data captured before and after the axial compression ϵ_0. The normalized cross-correlation image (CC) was used as a binary filter (pixels over 0.65 were kept) to prevent some bad estimated displacement data.

B. SPATIAL COMPOUNDING METHOD

The spatial compounding process was performed by considering the distance $h_s = 3$ cm between the rotation axis $O^{rotation}$, and the US probe coordinate system O^α, which introduces a translation on both the x-axis and z-axis. Further, this compounding process incorporates the axial translation given by $u_p^\alpha = (W/2)\tan(\alpha)$ of the US probe coordinate system O^α along the z-axis introduced by the pre-compression factor ϵ_p^α (not showed in the Figure 2b). Thus, both translations are computed by using the following equations:

$$T_{x,\alpha} = h_s \sin\alpha \tag{1}$$

$$T_{z,\alpha} = -h_s(1 - \cos\alpha) + u_p^\alpha \tag{2}$$

Figure 2b shows a schematic of the coordinate systems corresponding to our experimental setup. For each angle α, the US probe system of coordinates O^α is identified by the unitary vectors $\hat{u}_\alpha$ and $\hat{u}_\alpha^T$, and the displacement images by $u_{x,\alpha}$ and $u_{z,\alpha}$ (Figure 3a and 3b). Our experiments used small values of the US probe angular amplitude α_{max} to reduce the effect on the inclusion bonding condition described in [19]. The number of displacement images in the compounding process was controlled by the angular step $\Delta\alpha$. Thus, the compounding process translates to a non-rotated coordinated system O^0 and adds these low-resolution displacement images $u_{x,\alpha}$ and $u_{z,\alpha}$ by considering the translations introduced by the distance to the rotation axis h_s and the pre-compression factor ϵ_p^α. As a result, we estimate the high-resolution displacement images denoted by d_x and d_z, which are shown in Figures 3c and 3d, respectively. The relation between both coordinate systems is given by:

$$u_{x,\alpha} = \vec{d} \cdot \hat{u}_\alpha = d_x \cos\alpha - d_z \sin\alpha + T_{x,\alpha} \tag{3}$$

$$u_{z,\alpha} = \vec{d} \cdot \hat{u}_\alpha^T = d_x \sin\alpha + d_z \cos\alpha + T_{z,\alpha}. \tag{4}$$

Considering a set of many US probe angles, we can write the above equations as follows:

$$\vec{u} = A\vec{d} + \vec{T} + \vec{n}, \tag{5}$$

where $\vec{u}$ represents the pair of the observed displacements images $u_{x,\alpha}$ and $u_{z,\alpha}$ at different US probe angles α within the range $[-\alpha_{max}, +\alpha_{max}]$. A is the transformation matrix between the US probe coordinated system and the non-rotated coordinated system O^0. $\vec{T}$ is the translation vector given by the Eqs. 1, 2. $\vec{n}$ is the noise contribution of the displacement images along each scanning angle α. $\vec{d}$ is the high-resolution displacement image with components d_x and d_z at the non-rotated coordinated system O^0 as results of the spatial image compounding process [1], [2], [26]. The

description of these variables is shown below:

$$\vec{u} = \begin{pmatrix} U_{x,-\alpha_{max}} \\ \vdots \\ U_{x\alpha_i} \\ \vdots \\ U_{x,\alpha_{max}} \\ U_{z,-\alpha_{max}} \\ \vdots \\ U_{z,\alpha_i} \\ \vdots \\ U_{z,\alpha_{max}} \end{pmatrix},$$

$$A = \begin{pmatrix} \cos(-\alpha_{max}) & \sin(-\alpha_{max}) \\ \vdots & \vdots \\ \cos(\alpha_i) & \sin(\alpha_i) \\ \vdots & \vdots \\ \cos(\alpha_{max}) & \sin(\alpha_{max}) \\ -\sin(-\alpha_{max}) & \cos(-\alpha_{max}) \\ \vdots & \vdots \\ -\sin(\alpha_i) & \cos(\alpha_i) \\ \vdots & \vdots \\ -\sin(\alpha_{max}) & \cos(\alpha_{max}) \end{pmatrix},$$

$$\vec{T} = \begin{pmatrix} h_s \sin(-\alpha_{max}) \\ \vdots \\ h_s \sin(\alpha_i) \\ \vdots \\ h_s \sin(\alpha_{max}) \\ -h_s(1-\cos(-\alpha_{max})) + (W/2)\tan(-\alpha_{max}) \\ \vdots \\ -h_s(1-\cos(\alpha_i)) + (W/2)\tan(\alpha_i) \\ \vdots \\ -h_s(1-\cos(\alpha_{max})) + (W/2)\tan(\alpha_{max}) \end{pmatrix},$$

and $\vec{d} = \begin{pmatrix} d_x \\ d_z \end{pmatrix}$.

The inversion of Eq. 5 is given by:

$$\vec{d} = \left(A^T A\right)^{-1} A^T(\vec{u} - \vec{T} - \vec{n}) \approx \left(A^T A\right)^{-1} A^T(\vec{u} - \vec{T}), \quad (6)$$

where the elastographic noise term $\vec{n}$ is independent of the angle α and then is considered to vanish when the compounding is performed.

C. ROTATION ELASTOGRAM AND SHEAR STRAIN ELASTOGRAM

Once the high-resolution displacement was obtained through Eq. 6, the RE images were computed as:

$$\omega_{zx} = \frac{1}{2}\left(\frac{\partial d_z}{\partial x} - \frac{\partial d_x}{\partial z}\right). \quad (7)$$

Note that to compute the RE images using Eq. 7, the staggered method, described in [27], was utilized to reduce the noise from the gradient operation:

Similarly, the improvement of the resolution in the lateral displacement facilitates computing the *SSE* image as:

$$\epsilon_{zx} = \frac{1}{2}\left(\frac{\partial d_z}{\partial x} + \frac{\partial d_x}{\partial z}\right). \quad (8)$$

The quality of both *RE* and *SSE* images were quantified by the CNR_e parameter, defined as:

$$CNR_e = \frac{2\,(m_i - m_o)^2}{\left(\sigma_i^2 + \sigma_o^2\right)}. \quad (9)$$

Here, m_i and m_o are the average ω_{zx} (or ϵ_{zx}) values within a specific area inside and outside the lesion, respectively, and σ_i and σ_o are their respective standard deviation values [2], [12], [26] that characterize the variability of ω_{zx} (or ϵ_{zx}). To define these (*RE* or *SSE*) image areas, the lesion contour was first manually outlined from the axial strain elastrogram image (*ASE* image) (Figure 4a) and then was moved up along the axial direction to define the outside lesion area (Figure 4b). These areas are used to define two binary filters to compute the m_i and m_o values of the *RE* image (or *SSE* image) with their respective variances (Figures 4c and 4d).

III. RESULTS

We have performed two experiments of the spatial compounding process by using a loosely-bound elliptical inclusion with an inclination of $\approx 45°$. For the first experiment, we consider a maximal angular compounding amplitude of $\alpha_{max} = 1.5°$ and a step of $\Delta\alpha = 0.2°$ (15 displacement images). For the second experiment the values were $\alpha_{max} = 1°$, and $\Delta\alpha = 0.02°$ (100 displacement images). An orientation of $\approx 45°$ of the elliptical inclusion was used to maximize the rotation behavior. The inclusion was released for each US probe angle by translating the US probe until the loss of contact with the phantom and manually moving the inclusion. This last process was used to eliminate any adhesive behavior on the inclusion as a consequence of the previous manipulation, thus ensuring its free rotation for each new US probe angle.

Figure 5 shows the results of the spatial compounding process for the second experiment at different angular amplitudes ranging from $\alpha_{max} = 0°$ (top images, without compounding) to $\alpha_{max} = 1°$ (bottom images). Figure 5a) and b) depicts the high-resolution lateral displacement images d_x, and their respective *RE* images. Qualitatively, we can observe that the compounding process gradually increases the quality of the displacement image d_x, and the rotation fill-in signature becomes visible on the *RE* image, meaning that the contrast improves while the angular amplitude increases. Additionally, we note that the elastographic noise in the *RE* image was reduced, as described by the term $\vec{n}$ in Eq. 6.

To quantify the improvement of the rotation fill-in signature on *RE* images due to the mechanically assisted spatial compounding method technique, we compute the

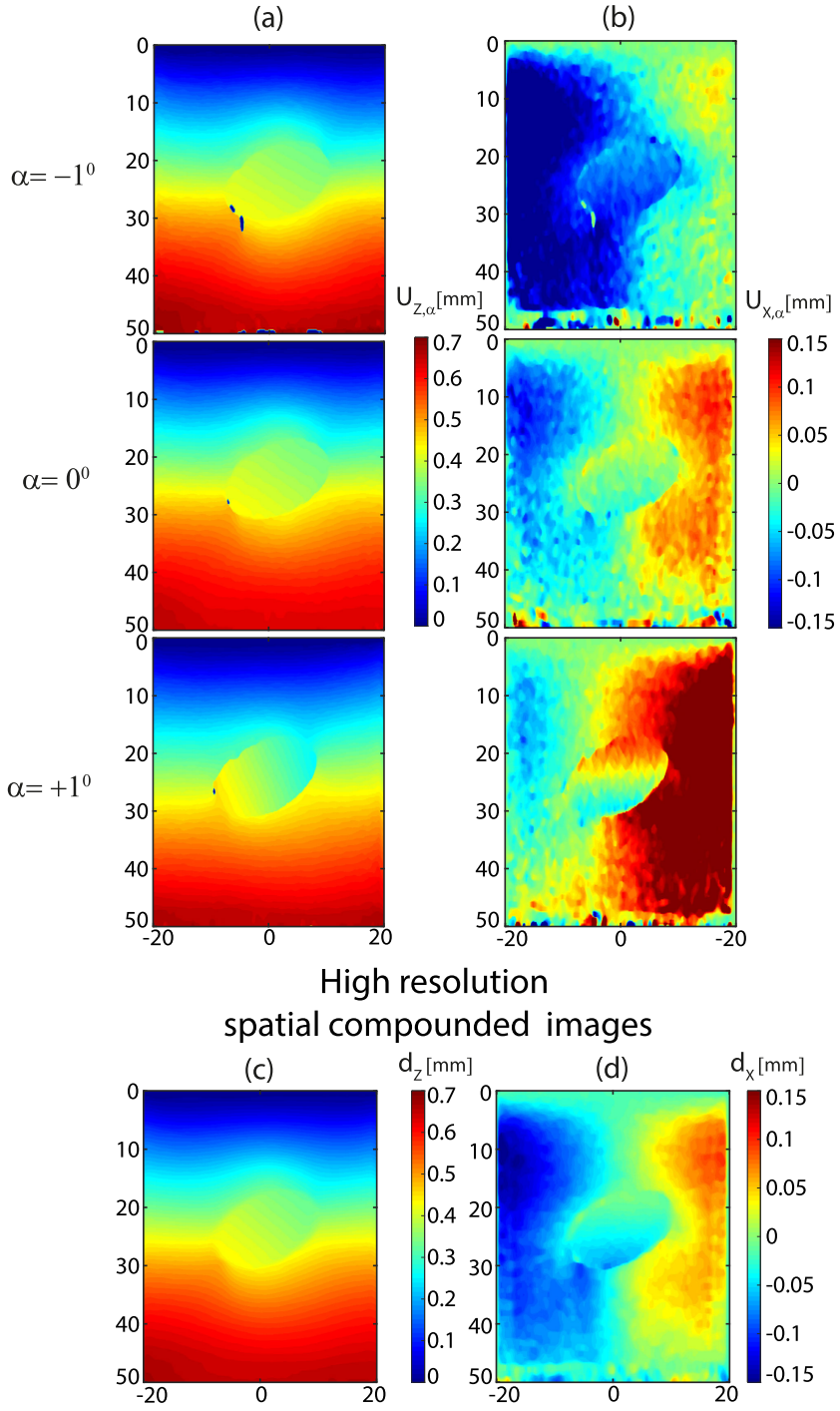

FIGURE 3. Spatial image compounding process.(a) Low resolution axial displacements images, $u_{z,\alpha}$ at 3 different US probe angles; from top to bottom $\alpha = -\alpha_{max} = -1°$, $\alpha = 0$, and $\alpha = +\alpha_{max} = 1°$. (b) Corresponding low-resolution lateral displacement images at the same US probe angles. (c) High-resolution axial displacement image d_z.(d) High-resolution lateral displacement image d_x. These last two images are produced by the spatial image compounding process of several displacement images ranging between $[-\alpha_{max}, +\alpha_{max}]$.

contrast-to-noise ratio CNR_e, described by Eq. 9. Figure 6a shows the CNR_e as a function of angular compounding amplitude α_{max} for both above experiments ($\Delta\alpha = 0.2°$ and $\Delta\alpha = 0.02°$). The lesion outline was manually obtained and is shown in Figure 4. The same outline was used for all α_{max} values. At $\alpha_{max} = 1°$, we observe a contrast amelioration of 2 dB for the first experiment ($\Delta\alpha = 0.2°$) and a more relevant improvement of 5 dB for the second one ($\Delta\alpha =$

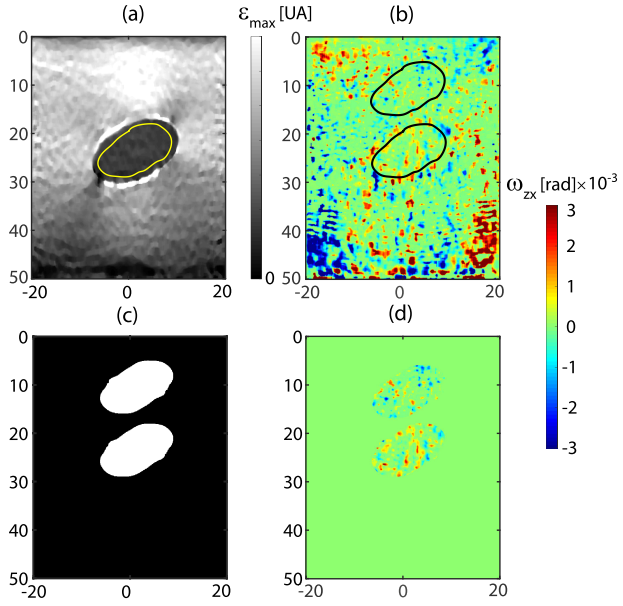

FIGURE 4. Contrast-to-noise estimation (CNR_e).(a) *ASE* Image with lesion contour (yellow line). (b) *RE* image with the lesion (black) and the background (white) outlines. This was obtained by axially moving the lesion outline. (c) A binary image was computed from the lesion and background outline. (d) Masking of *RE* image lesion and background areas. The (c) and (d) images are only representatives of the masking process. In fact, both the lesion and background areas are processed separately.

0.02°). This result is consistent with our simulation study [19] (see segmented lines in Figure 6a), and shows that the use of more displacement images in the compounding process reduces the noise term ($\vec{n}$). Figure 6b shows the averaged values of $m_i = \omega_{zx}$ inside the lesion for both experiments. Error bars represent the standard deviation values σ_i. In this curve, we can observe that, while the average value of m_i reaches 4×10^{-4} rad, the elastographic noise was reduced by a factor of almost 3. This shows that the noise reduction (by increasing the number of displacement images) controls the contrast enhancement of the *RE* image over the angular compounding amplitude α_{max}.

IV. DISCUSSION

The experimental study presented here demonstrates that improving the *RE* image quality is technically feasible by compound displacement images from different US probe angles, which validates our previous simulation results [19]. Our results (see Figure 6a) show that the contrast-to-noise CNR_e enhancement of the rotation signature as a function of the angular compounding amplitude α_{max} follows the prediction done by our numerical study ([19]), it means the CNR_e can be improved for small range of scanning angles α_{max} if we increase the number of displacement images. In fact our results, shown an improvement of 2 dB for $\alpha_{max} = 1.5°$, using 30 displacement images ($\Delta\alpha = 0.2°$) and 5 dB for $\alpha_{max} = 1°$, using 100 displacement images ($\Delta\alpha = 0.02°$). These results are comparable with the numerical results presented previously in [19], despite the difference between the axis of rotation used in both studies and the fact that the simulation study does not consider the bonding dependence of the pre-stress distribution introduced by the US probe when a pre-compression u_p^{α} is applied. Note that this behavior can limit the inclusion rotation, reducing the performance of the spatial image compounding ([23]). The introduction of this scenario in our simulation requires a suitable bonding model that considers a pre-stress dependence. For this reason, we have focused our study on the *RE* image quality improvement for small angles ($\alpha_{max} = 1.5°$), and we showed that the CNR_e could be enhanced by reducing the angular step size $\Delta\alpha$, (namely, by increasing the number of displacement images used in the spatial compounding). This can be intuitively understood if we consider that the spatial compounding is actually an average of displacement images, where the elastographic noise $\vec{n}$ is reduced during the averaging process (see 6). This can be visualized in Figure 6b, where the average ω_{zx} value inside the inclusion reaches a plateau, showing that the pre-compression does not modify the bonding nature of the inclusion, while the standard deviation is reduced by a factor of 3. The observed top corner artifacts may arise from the absence of a perfectly sliding condition of the compression plate and/or from its size, which is smaller than the sample width, introducing an undesirable shearing behavior around its corners. To avoid this, it is necessary to lubricate the compression plate and increase its size. We know that using larger angles with a coarse step may be more suitable for clinical translation, but using larger angles needs a greater pre-compression, which is challenging to perform experimentally. Additionally, using larger angles with a coarse step will not necessarily enhance the rotational fill-in. In fact, our simulations for amplitude angle of 10° using a scanning step of 0.2° (100 displacement images) predict an improvement of 6 dB. Nevertheless, a trade-off between the amplitude angle and the angular stepping would allow the rotational contrast to improve further, enabling the computation of the rotational under in-vivo conditions.

We note that the quality improvements on the rotational elastogram images described here are consistent with previous studies using angular imaging compounding methods with beamforming techniques such as beam-steering [9], [10], [11], [12], [13], but without the physical limitations of angular sensitivity of the linear array used in breast tumor scanning. Furthermore, access to the lateral displacements allows the computation of other types of elastograms, such as the lateral strain and shear strain (8). This last, in addition to the rotation elastogram may be important if we want to compare the rotation ability of a lesion with its shearing nature. In fact, the *SSE* image, ϵ_{zx}, is shown in Figure 7a, where we can observe shearing fill-in, which reveals that the inclusion is not absolutely free of rotation. The co-existence of rotation and shearing also explains the reason why the rotation variability is larger. It means, despite the rotation fill-in is improved, its mean value is actually small, 2-4x10^{-4} rad, making that its variability became relevant. The

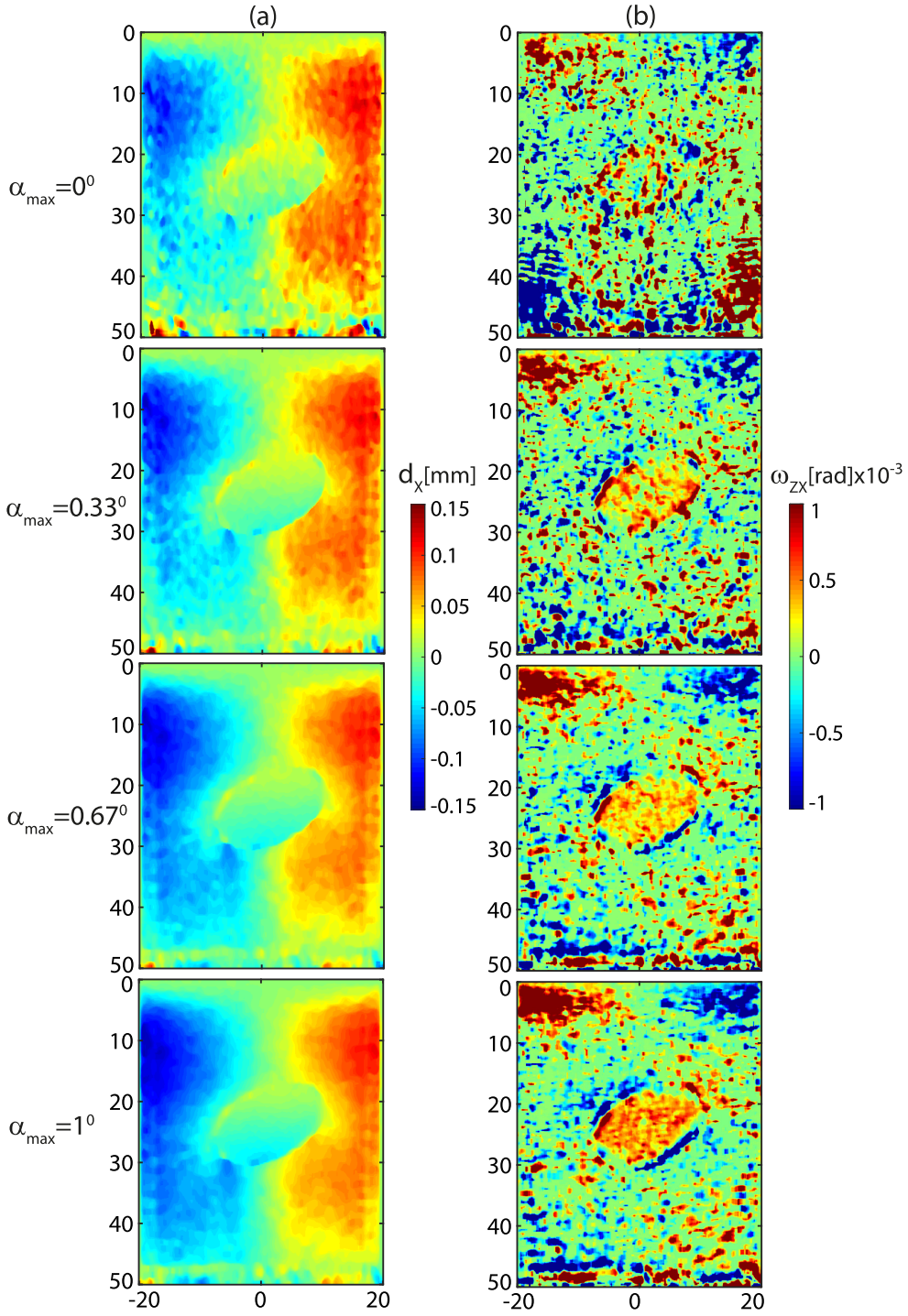

FIGURE 5. ***RE*** **images obtained from the high resolution displacement images d_z and d_x for different angular scanning amplitude α_{max} using an angular scanning step of 0.02° (100 images). (a) High resolution lateral displacement images d_x for $\alpha_{max} = 0,\ 0.33,\ 0.67$ and 1° (top to bottom). (b) Corresponding *RE* images computed by applying 7.**

improvements in shear strain image quality as a function of angular amplitude α_{max} are shown in Figure 7b, where it can be seen a similar behavior than the observed for the rotation elastogram (Figure 6b). The existence of both behavior, rotation and shearing, explains why the rotation signature is not as notorious as in other studies and allows us to define a new parameter to quantify the rotation ability of the inclusion with respect to its shearing nature. To do this, we compute the ratio between the average rotation with respect to the average shear strain fill-ins of the inclusion as a function of

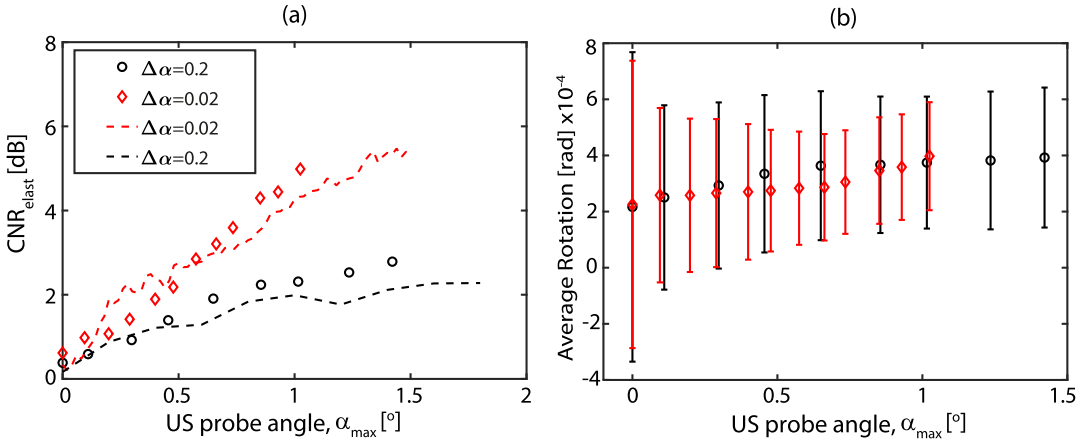

FIGURE 6. Contrast-to-noise enhancement CNR_e and average ω_{zx} values. (a) CNR_e values as function of the angular scanning amplitude α_{max} for two values of the angular scanning step 0.2 and 0.02° (black circles and red diamonds). The segmented lines correspond to the simulation results described in [19]. (b) average ω_{zx} values inside the lesion, m_i, as function of the angular scanning amplitude α_{max} for an angular scanning step of 0.02°. The error bars represent the standard deviation values σ_i.

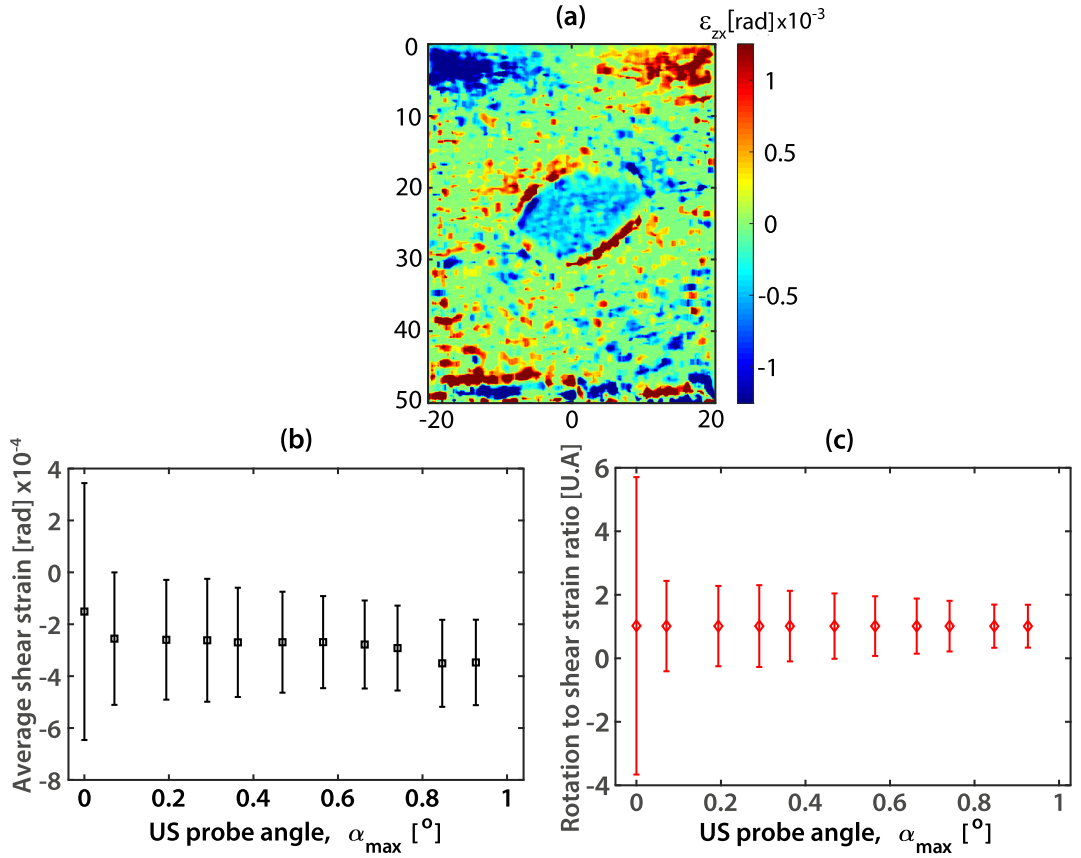

FIGURE 7. *SSE* image (8) and rotation to shear strain ratio inside the inclusion. (a) ϵ_{zx} estimated from the high resolution displacements images for $\alpha_{max} = 1\circ$ and an angular scanning step of 0.02°. (b) average ϵ_{zx} values inside the inclusion as a function of the angular scanning amplitude α_{max}. (c) ratio between the average ω_{zx} and average ϵ_{zx} values inside the inclusion. The error bars represent the standard deviation values.

angular amplitude α_{max}, see Figure 7c. We observe a more drastic reduction of the error bars and a more stable behavior of the mean values as a function of angular amplitude α_{max}, showing that this parameter may be more robust than rotation and shear strain fill-in separately. However, more exhaustive studies are necessary to evaluate if this parameter is more suitable to differentiate between loosely and firmly bounded inclusions.

The in-vivo application of this spatial compounding during hand-held US scanning procedure requires a real-time, measuring of the US probe angle and position, synchronized with the *RE* image in in-vivo calculation. This could be technically hard to address because it is necessary to capture the US probe angle and position with high precision, which implies the use of a small scanning step (larger amount of displacement images) to improve the rotational and to compensate the US probe coordinate system position for any movement of the US probe along with a real-time feedback guidance procedure for the hand-held *RE* image quality enhancement. Nevertheless, we believe that this method may be more suitable to be implemented in conjunction with techniques such as robotic palpation [28], [29], where the motion of the ultrasound probe can be achieved accurately through the use of a robotic system while the elastographic images are estimated or by incorporating internal actuators within the ultrasound probe, like was described in [13] for sub-pitch approach to overcome the lateral resolution limitations. Whatever the approach, we think it may be relevant for the translation of this ultrasonic technique to situations or regions where the use of inexpensive imaging technology and/or portable ultrasound equipment is necessary. However, finding the optimal trade-off between the stepping angle and the angular amplitude would enable the election of one of these approaches. Even though the clinical significance of this study is limited in comparison with studies were Young's modulus, Poisson's ratio, and others parameters, are estimated [30], [31], [32], the rotation elastogram is a direct estimation of the macro-mechanical behavior of benign tumors as fibroadenomas and may be used as a complementary parameter to improve the breast tumor diagnosis using ultrasound elastography. Furthermore, the use of machine and deep learning methods can improve tissue motion estimation, which can become relevant for enhancing the quality of *RE* image [33].

V. CONCLUSION

In summary, we have demonstrated that it is technically feasible to improve the rotation elastogram image quality for small angular amplitude values α_{max} if the number of displacement images used during the spatial image compounding is increased, which reduces the elastographic noise during the compounding process. Despite some differences between simulations and experimental methodologies, the experimental results confirm the prediction of our simulation study. However, its clinical applicability requires an exhaustive US probe position control synchronized with the US image acquisition process.

ACKNOWLEDGMENT

The authors are grateful to Carolina Ordenes for the development of the schematic of Figure 2b.

REFERENCES

[1] U. Techavipoo, Q. Chen, T. Varghese, and J. A. Zagzebski, "Estimation of displacement vectors and strain tensors in elastography using angular insonifications," *IEEE Trans. Med. Imag.*, vol. 23, no. 12, pp. 1479–1489, Dec. 2004.

[2] C. Sowmiya, A. A. Kothawala, and A. K. Thittai, "Rotation elastogram: A novel method to visualize local rigid body rotation under quasi-static compression," in *Medical Imaging: Ultrasonic Imaging and Tomography*. Bellingham, WA, USA: SPIE, 2016.

[3] A. K. Thittai, B. Galaz, and J. Ophir, "Axial–Shear strain distributions in an elliptical inclusion model: Experimental validation and in vivo examples with implications to breast tumor classification," *Ultrasound Med. Biol.*, vol. 36, no. 5, pp. 814–820, May 2010.

[4] H. Xu, M. Rao, T. Varghese, A. Sommer, S. Baker, T. J. Hall, G. A. Sisney, and E. S. Burnside, "Axial-shear strain imaging for differentiating benign and malignant breast masses," *Ultrasound Med. Biol.*, vol. 36, no. 11, pp. 1813–1824, Nov. 2010.

[5] A. K. Thittai, B. Galaz, and J. Ophir, "On the advantages of imaging the axial-shear strain component of the total shear strain in breast tumors," *Ultrasound Med. Biol.*, vol. 38, no. 11, pp. 2031–2037, Nov. 2012.

[6] B. D. Fornage, J. G. Lorigan, and E. Andry, "Fibroadenoma of the breast: Sonographic appearance," *Radiology*, vol. 172, no. 3, pp. 671–675, Sep. 1989.

[7] S. A. Salati, "Breast fibroadenomas: A review in the light of current literature," *Polish J. Surgery*, vol. 93, no. 3, pp. 1–5, May 2021.

[8] B. Galaz, A. ThitaiKumar, and J. Ophir, "Axial-shear strain distributions in an elliptical inclusion model (Part I): A simulation study," in *Proc. Int. Conf. Ultrason. Meas. Imag. Tissue Elasticity*, 2009, p. 99.

[9] B. R. Chintada and A. K. Thittai, "Rotation elastogram estimation using synthetic transmit-aperture technique: A feasibility study," *Ultrason. Imag.*, vol. 39, no. 3, pp. 189–204, May 2017.

[10] A. Kothawala, S. Chandramoorthi, N. R. K. Reddy, and A. K. Thittai, "Spatial compounding technique to obtain rotation elastogram: A feasibility study," *Ultrasound Med. Biol.*, vol. 43, no. 6, pp. 1290–1301, Jun. 2017.

[11] B. Lokesh and A. K. Thittai, "Diverging beam with synthetic aperture technique for rotation elastography: Preliminary experimental results," *Phys. Med. Biol.*, vol. 63, no. 20, Oct. 2018, Art. no. 20LT01.

[12] S. Selladurai and A. K. Thittai, "Strategies to obtain subpitch precision in lateral motion estimation in ultrasound elastography," *IEEE Trans. Ultrason., Ferroelectr., Freq. Control*, vol. 65, no. 3, pp. 448–456, Mar. 2018.

[13] S. Selladurai and A. K. Thittai, "Actuator-assisted subpitch translation-capable transducer for elastography: Preliminary performance assessment," *Ultrason. Imag.*, vol. 42, no. 1, pp. 15–26, Jan. 2020.

[14] M. T. Islam, A. Chaudhry, S. Tang, E. Tasciotti, and R. Righetti, "A new method for estimating the effective Poisson's ratio in ultrasound poroelastography," *IEEE Trans. Med. Imag.*, vol. 37, no. 5, pp. 1178–1191, May 2018.

[15] M. T. Islam and R. Righetti, "A novel filter for accurate estimation of fluid pressure and fluid velocity using poroelastography," *Comput. Biol. Med.*, vol. 101, pp. 90–99, Oct. 2018.

[16] H. Liebgott, A. Basarab, P. Gueth, D. Friboulet, and P. Delachartre, "Transverse oscillations for tissue motion estimation," *Ultrasonics*, vol. 50, no. 6, pp. 548–555, May 2010.

[17] F. Varray and H. Liebgott, "An alternative method to classical beamforming for transverse oscillation images: Application to elastography," in *Proc. IEEE 10th Int. Symp. Biomed. Imag.*, Apr. 2013, pp. 716–719.

[18] A.-L. Duroy, V. Detti, A. Coulon, O. Basset, and E. Brusseau, "Regularization-based 2D strain tensor imaging in quasi-static ultrasound elastography SAGE publications," *Ultrason. Imag.*, vol. 45, no. 4, pp. 187–205, Jul. 2023.

[19] B. Galaz, T. Henriquez, D. Espíndola, and M. Trejo, "Rotation elastogram estimation using mechanical assisted spatial compounding: A simulation study," in *Proc. IEEE UFFC Latin Amer. Ultrason. Symp. (LAUS)*, Oct. 2021, pp. 1–4.

[20] M. H. Choi and M. H. Bae, "Spatial compounding of ultrasonic diagnostic images for rotating linear probe with geometric parameter error compensation," *J. Electr. Eng. Technol.*, vol. 9, no. 4, pp. 1418–1425, Jul. 2014.

[21] J. A. Jensen and N. B. Svendsen, "Calculation of pressure fields from arbitrarily shaped, apodized, and excited ultrasound transducers," *IEEE Trans. Ultrason., Ferroelectr., Freq. Control*, vol. 39, no. 2, pp. 262–267, Mar. 1992.
[22] J. A. Jensen, "FIELD: A program for simulating ultrasound systems," in *Proc. IEEE 10th Nordic-Baltic Conf. Biomed. Imag.*, vol. 34, Mar. 1996, pp. 351–353.
[23] B. Galaz, E. Donoso, and M. Trejo, "Importance of the ultrasound probe angle on the rotation fill-in signature in ultrasound axial-shear strain imaging," *Ultrasound Med. Biol.*, vol. 47, no. 2, pp. 345–354, Feb. 2021.
[24] F. Kallel, C. D. Prihoda, and J. Ophir, "Contrast-transfer efficiency for continuously varying tissue moduli: Simulation and phantom validation," *Ultrasound Med. Biol.*, vol. 27, no. 8, pp. 1115–1125, Aug. 2001.
[25] A. K. Thittai, B. Galaz, and J. Ophir, "Importance of axial compression verification to correct interpretation of axial-shear strain elastograms in breast lesions," *Ultrason. Imag.*, vol. 32, no. 3, pp. 190–198, Jul. 2010.
[26] H. Xu and T. Varghese, "Normal and shear strain imaging using 2D deformation tracking on beam steered linear array datasets," *Med. Phys.*, vol. 40, no. 1, Jan. 2013, Art. no. 012902.
[27] S. Srinivasan, J. Ophir, and S. Alam, "Elastographic imaging using staggered strain estimates," *Ultrasonic Imaging*, vol. 24, no. 4, pp. 229–245, 2002.
[28] P. A. Patlan-Rosales and A. Krupa, "Automatic palpation for quantitative ultrasound elastography by visual servoing and force control," in *Proc. IEEE/RSJ Int. Conf. Intell. Robots Syst. (IROS)*, Oct. 2016, pp. 2357–2362.
[29] P. A. Patlan-Rosales and A. Krupa, "Robotic assistance for ultrasound elastography providing autonomous palpation with teleoperation and haptic feedback capabilities," in *Proc. 8th IEEE RAS/EMBS Int. Conf. Biomed. Robot. Biomechatronics*, Nov. 2020, pp. 1018–1023.
[30] M. T. Islam, E. Tasciotti, and R. Righetti, "Estimation of vascular permeability in irregularly shaped cancers using ultrasound poroelastography," *IEEE Trans. Biomed. Eng.*, vol. 67, no. 4, pp. 1083–1096, Apr. 2020.
[31] M. T. Islam, S. Tang, C. Liverani, S. Saha, E. Tasciotti, and R. Righetti, "Non-invasive imaging of young's modulus and Poisson's ratio in cancers in vivo," *Sci. Rep.*, vol. 10, no. 1, p. 7266, Apr. 2020.
[32] M. T. Islam, S. Tang, E. Tasciotti, and R. Righetti, "Non-invasive assessment of the spatial and temporal distributions of interstitial fluid pressure," *IEEE Access*, vol. 9, pp. 89222–89233, 2021.
[33] H. Li, M. Bhatt, Z. Qu, S. Zhang, M. C. Hartel, A. Khademhosseini, and G. Cloutier, "Deep learning in ultrasound elastography imaging: A review," *Med. Phys.*, vol. 49, no. 9, pp. 5993–6018, Sep. 2022.

TERESA ZAGAGLIONI was born in Santiago, Chile, in 1992. She received the bachelor's degree in applied physics from Universidad de Santiago de Chile, in 2019. From 2017 to 2023, she was a Research Assistant with the Physics Department, University of Santiago of Chile, where she conducted research work on the improvement of the rotation elastogram imaging quality with Prof. Belfor A. Galaz. In 2019, she participated in the Annual Congress of Biomedical Engineering of Universidad de Concepción, where she showed some advances in her work on ultrasound elastography. Also, she was with the Calibration Laboratory DTS, Santiago, where she was trained in the interpretation and analysis of ISO 9001:2015 and ISO 17025:2017 Standards.

MIGUEL TREJO was born in Santiago, Chile, in 1980. He received the Ph.D. degree in physics from Université Pierre et Marie Curie, Paris, France, in 2010. During the Ph.D. degree, he was with the Laboratoire de Physique Statistique (LPS), ENS, Paris, where he studied the geometry and mechanics of fluid and elastic membranes. After finishing the Ph.D. degree, he pursued a first postdoctoral position with LPS, Universite Paris-Sud, Orsay, France. He worked on the mechanical properties of soft bacterial biofilms. In 2012, he held a second postdoctoral position with the Laboratoire Sciences et Ingénierie de la Matière Molle (SIMM), ESPCI, Paris, where he worked on the frictional, adhesive, and mechanical properties of soft viscoelastic polymers. In 2013, he was an Assistant Professor with the Laboratoire PMMH, ESPCI. In 2019, he was a CONICET Researcher with the Laboratorio de Interacción Fluido-Estructura y Materia Activada (LIFEMA), Instituto de Física de Buenos Aires (IFIBA), Buenos Aires, Argentina. His research focused on different subjects related to the mechanics and physics of soft matter. His current research interests include friction, adhesion, elasticity, and mechanics of synthetic and living soft matter, with applications in ultrasound imaging, biomechanics, morphogenesis, and bioinspired active materials.

DAVID A. ESPÍNDOLA was born in Chillán, Chile, in 1986. He received the Ph.D. degree in physics from Universidad de Santiago de Chile, Santiago, Chile, in 2012. As part of his Ph.D. dissertation, he studied the interaction of wave particles in granular materials. He pursued postdoctoral research with the Institut d'Alembert, Sorbonne University, Paris, France, where he started conducting research on medical ultrasound. He also held a postdoctoral position with The University of North Carolina at Chapel Hill, Chapel Hill, NC, USA, where he was a Research Assistant Professor, until 2019. He is currently an Associate Professor with the Instituto de Ciencias de la Ingeniería, Universidad de O'Higgins, Rancagua, Chile. His current research interests include linear and nonlinear shear wave propagation in soft tissue, the design of novel ultrasound sequences for the development of quantitative images, and the improvement of vascular imaging using ultrasound super-resolution techniques.

BELFOR A. GALAZ was born in Santiago, Chile, in 1979. He received the dual Ph.D. degree in physics from Universidad de Santiago de Chile, Santiago, and Université Pierre et Marie Curie, Paris, France, in 2009, as part of the Cotutelle Program. During the Ph.D. degree, he was with the Laboratoire dÍmagerie Biomédicale. He studies the ultrasonic characterization of micro and nanoemulsions of liquid perfluorocarbon as contrast agents. After finishing the Ph.D. degree, he pursued postdoctoral research with The University of Texas Health Science Center at Houston, Houston, TX, USA, where he started conducting research on quasi-static ultrasound elastography with Prof. Jonathan Ophir. Since 2010, he has been a Professor with the Departamento de Física, Universidad de Santiago de Chile, where his current research interests include ultrasound elastography imaging and the study of complex solids through ultrasonic diffuse waves.